Geodynamic Modeling with Uncertain Initial Geometries

A. Spang [1], T. S. Baumann [1], B. J. P. Kaus [1,2]

[1]Johannes Gutenberg University, Institute of Geosciences, Johann-Joachim-Becher-Weg 21, 55128 Mainz, Germany

[2]TeMaS, Terrestrial Magmatic Systems Research Center, temas.uni-mainz.de

Key Points:

- New, simple, intuitive and open-source method to describe and manipulate complex 3D bodies with a small number of parameters
- Allows for the integration of uncertainties of the initial geometry and enables inverting for geometric properties in numerical models
- Applications to a salt diapir with uncertain intial geometry and a subduction zone with uncertain initial subduction angle

Corresponding author: Arne Spang, `arspang@uni-mainz.de`

Abstract

Geodynamic codes have become fast and efficient enough to facilitate sensitivity analysis of rheological parameters. With sufficient data, they can even be inverted for. Yet, the geodynamic inverse problem is often regularized by assuming a constant geometry of the geological setting (e.g. shape, location and size of salt diapirs or magma bodies) as parameterization of complex 3D shapes involves too many parameters. A common solution of this issue is the approximation of irregular bodies with simple shapes like boxes, spheres or ellipsoids. Here, we present a simple and intuitive method to parameterize complex 3D bodies and incorporate them into geodynamic inverse problems. The approach can automatically create an entire ensemble of initial geometries, enabling us to account for uncertainties in imaging data. Furthermore, it allows us to investigate the sensitivity of the model results to geometrical properties and facilitates inverting for them. We demonstrate the method with two examples. A salt diapir in an extending regime and free subduction of an oceanic plate under a continent. In both cases, small differences in the model's initial geometry lead to vastly different results. Be it the formation of faults or the velocity of plates. Using the salt diapir example, we demonstrate that, given an additional geophysical observation, we are able to invert for uncertain geometric properties. This highlights that geodynamic studies should investigate the sensitivity of their models to the initial geometry and include it in their inversion framework. We make our method available as part of the open-source software geomIO.

Plain Language Summary

Computer models of geological settings have become a popular tool of research. They require the user to provide information on where the different geological units (rock layers, salt domes, magma bodies etc.) start and end as well as material parameters like density and strength of the units. As many of these input parameters are not well known, a lot of studies run multiple simulations with different parameter combinations to investigate the influence the individual parameters and their uncertainties have. However, the initial geometry often remains fixed as it is difficult to describe with only few parameters and therefore unrealistic to vary. Here, we present a new method to describe and manipulate the geometry of geological units with a small number of parameters. This allows us to also vary the initial geometry and investigate how the model results depend on it. We apply our method to a salt diapir and a subduction zone to demonstrate the

impact of initial geometry on the simulation results. To make our method available to the community, we implement it as a tool into geomIO, an open-source software package to generate initial geometries for geodynamic models.

Index Terms

1976 Software tools and services

0545 Modeling

8118 Dynamics and mechanics of faulting

8170 Subduction zone processes

3275 Uncertainty quantification

Keywords

Geometry Parameterization, Variable Geometry, Salt Tectonics, Subduction Velocity, Inversion, Subduction Angle

1 Introduction

Numerical modeling has become a powerful tool to investigate how different mechanical and thermodynamical parameters influence and control geological systems such as orogens, subduction zones, magmatic systems, basins and other terrestrial bodies (Baumann et al., 2014; Baumann & Kaus, 2015; Ratnaswamy et al., 2015; Reuber et al., 2018). With the help of observations, we can constrain rheology, density and thermal properties of geological units with forward and inverse approaches. The initial geometry of the model is, however, usually treated as a constant and not included in the parameter variation. This is because creating the initial geometry is, especially in three dimensions (3D), a time consuming process and parameterization is difficult if the shapes of the individual units are more complex than simple geometric bodies such as planes, boxes, spheres or ellipsoids. While material parameters can be defined with a small amount of numeric values, geometry is a large collection of coordinates. Because of that, many modeling studies do not only have to ignore the uncertainties that are associated with the initial geometry but also lose the ability to investigate the influence of the initial geometry on the model results.

Previous studies have tackled this problem in various ways. The open-source software package GemPy (e.g. Varga et al., 2019; Schaaf et al., 2021) allows the creation of interfaces like layered rock units or faults and supports the analysis of uncertainties. Sevilla et al. (2020) use the control points of NURBS surfaces for flexible closed 3D shapes. Galley et al. (2020) present the SGI method that directly varies the coordinates of certain surface vertices. The authors also provide an extensive overview over previous studies that find different ways of parameterizing the geometry of geological settings. A common issue of these approaches is the large number of parameters leading to an expensive inversion process and/or unintuitive nature of the parameters.

Here, we present a simple and intuitive method to manipulate complex 3D bodies (e.g. salt domes, magma bodies, subducting slabs) with a small number of numerical parameters. The method is implemented as a tool in the open-source package geomIO (Bauville and Baumann (2019), https://bitbucket.org/geomio/geomio) which allows for the creation of 3D initial geometric setups with vector graphic editors like Inkscape and is fully compatible with the thermomechanical code LaMEM (Kaus et al., 2016). This facilitates the inclusion of geometric uncertainties in geodynamic modeling and enables us to invert for geometric properties of subsurface geological features. In the following sections, we present the method and apply it to 2 different geological scenarios. (i) Seismic imaging of a salt daipir is associated with uncertainties regarding its horizontal and vertical extent. By modeling this diapir in an extending regime, we show that different initial geometries that lie within the uncertainty of the imaging study lead to significantly different faulting patterns. We identify which parts of the diapir's geometry have the largest influence on the developing faults. Using a synthetic observation, we demonstrate that it is possible to invert for the initial geometry of the diapir. (ii) We model free subduction of an oceanic plate underneath a continent and investigate the dependence of the velocities of both plates on the initial dip angle of the subducting slab. We also track the evolution of the dip angle as the plate subducts and compare the results to natural observations.

2 Methods

As the definition of any complex 3D shape requires a large number of coordinates, our method always needs a reference model or starting geometry, which may have any level of complexity. We then create parameters which describe a transformation of this

reference model into a different shape. Section 2.1 describes our general transformation algorithm applicable to any shape, and section 2.2 shows an example of how it can be used to transform a sphere into a more complex shape. Section 2.3 shows how the method can be adapted for a subduction setting.

2.1 Transformation Algorithm

2.1.1 Scaling Parameters

To manipulate the reference geometry, we compute the intersection of the 3D body with a finite number of horizontal planes. In a second step, we select a subset of the resulting two-dimensional (2D) polygons (red in Figure 1a), which are referred to as control polygons. For each of the control polygons (P_i) we define two scaling parameters (Sx_i and Sy_i) and compute scaling parameters for all other polygons in the following manner:

(i) Polygons below the lowermost control polygon copy its scaling parameters.
(ii) The scaling parameters of polygons between two control polygons are linearly interpolated between those of the control polygons.
(iii) Polygons above the uppermost control polygon copy its scaling parameters.

To achieve a homogeneous transformation in the horizontal plane, Sx_i must equal Sy_i which reduces the number of necessary parameters to one per control polygon. Finally, there is a single parameter (Sz) to transform the body in the vertical direction.

2.1.2 Vertical Scaling

To scale the body in the vertical direction, the spacing between the polygons is multiplied by the vertical scaling parameter (Sz):

$$z_{i,new} = (z_i - z_{ref}) * Sz + z_{ref} \tag{1}$$

Where z_i is the vertical coordinate of the polygon and z_{ref} is the reference depth of vertical scaling. If $Sz > 1$, the body is vertically extended, if $Sz < 1$, the body is shrunk. z_{ref} should be chosen in dependence of the object to be transformed. For shapes like magma

or ore bodies that are not bound to another unit, it makes sense to use the body's center of mass while for a salt diapir, its base is more appropriate.

2.1.3 Horizontal Scaling

To scale the body in the two horizontal directions, the following steps are applied to each polygon individually. First, we compute the position of the polygon's center of mass and transform the coordinates of all nodes on the polygon to be relative to it:

$$\begin{pmatrix} \vec{x_i}' & \vec{y_i}' \end{pmatrix} = \begin{pmatrix} \vec{x_i} & \vec{y_i} \end{pmatrix} - \begin{pmatrix} x_{i_c} & y_{i_c} \\ ... & \\ x_{i_c} & y_{i_c} \end{pmatrix} \tag{2}$$

Where $\vec{x_i}'$ and $\vec{y_i}'$ are vectors containing the relative coordinates of the nodes of the polygon, $\vec{x_i}$ and $\vec{y_i}$ are vectors containing the absolute coordinates of the nodes and x_{i_c} and y_{i_c} are the absolute coordinates of the polygon's center of mass. Then, all x-coordinates are multiplied by Sx_i and all y-coordinates by Sy_i. Lastly, the coordinates are transformed back into absolute values:

$$\begin{pmatrix} \vec{x}_{i,new} & \vec{y}_{i,new} \end{pmatrix} = \begin{pmatrix} \vec{x_i}' & \vec{y_i}' \end{pmatrix} * \begin{pmatrix} Sx_i & 0 \\ 0 & Sy_i \end{pmatrix} + \begin{pmatrix} x_{i_c} & y_{i_c} \\ ... & \\ x_{i_c} & y_{i_c} \end{pmatrix} \tag{3}$$

If $Sx_i > 1$, the polygon extends in x-direction and if $Sx_i < 1$, the polygon shrinks. The same is true for Sy_i and the y-direction.

2.1.4 Additional Options

Equations 1 - 3 are the core of our method and sufficient to describe all operations used in the following example and the application in section 3.1. Supplementary text S1 describes additional options that we implemented.

2.2 Example

For the sake of convenient visualization, we choose a sphere as our reference model. We represent the sphere with 21 equally spaced, horizontal polygons (Figure 1a) but the

number of plain intersections is arbitrary. Polygons 13, 15 and 19 are chosen to be control polygons (red in Figure 1a) and for each one we set the parameters Sx and Sy (red in table 1). The other scaling parameters are then computed according to section 2.1.1 and used to transform the sphere in Figure 1a into the shape shown in Figure 1b. As we did not specify a vertical scaling parameter Sz, the body does not change its height. Figure 1c shows another example using the same parameters of table 1 with $Sz = 0.6$.

The procedure can be imagined as pulling ($S > 1$) or pinching ($S < 1$) a rubber object at the locations of the control polygons. The only difference being, that the top and bottom of the object are not fixed but deform together with the closest control polygon. To keep top or bottom fixed, simply make the first (bottom) or last (top) polygon a control polygon with $S = 1$.

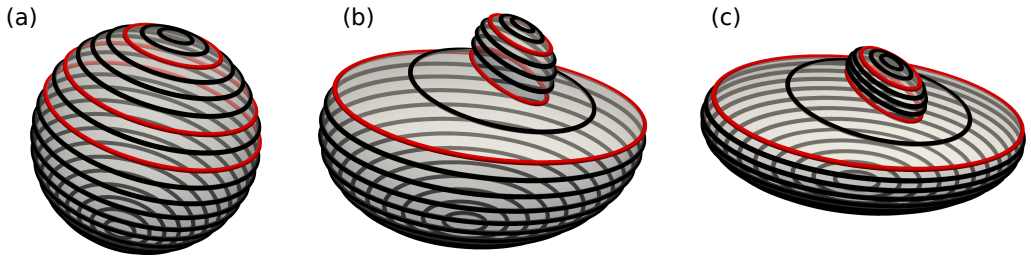

Figure 1. Illustration of 3D bodies as a set of 2D polygons. The three red slices are the control polygons which are used to transform the body. (a) Reference model sphere represented as horizontal polygons. (b) Sphere from 1a after transformation with the scaling parameters of table 1. (c) Sphere from 1a after transformation with $Sz = 0.6$ and the scaling parameters of table 1.

2.3 Subduction Zones

Subduction zones are frequently investigated in geodynamic modeling studies. A central element is the orientation and location of the subducting slab. In this case, it is more convenient to represent the subducting plate as a collection of vertical polygons (Figure 2). We automatically detect the polygon nodes that make up the slab part (red in Figure 2b) and rotate them by angle θ to change the subduction angle (blue in Figure 2b). For 3D slabs that dip obliquely to the orientation of the coordinate system (Figure 2a), we first detect the direction of dip and recalculate θ' in the plane of the polygons so that the entire slab is rotated correctly. Additional rotation centers can also be

Table 1. Scaling parameters used to transform the sphere in Figure 1a into the shapes in Figures 1b,c. Note that the polygon numbering goes from the bottom to the top. Only the red numbers are free parameters that need to be chosen. The black numbers are generated automatically, depending on the red ones.

Polygon	Sx	Sy
21	0.50	0.90
...	0.50	0.90
19	0.50	0.90
18	0.45	0.83
17	0.40	0.75
16	0.35	0.68
15	0.30	0.60
14	0.90	0.80
13	1.50	1.00
...	1.50	1.00
1	1.50	1.00

placed anywhere along the slab to bend the deeper parts (Figure S3). This can be useful when the dip of the slab is well constrained close to the surface but changes at depth like along the west coast of South America.

Subduction setups often require a weak zone of elevated temperature, lowered viscosity or lowered yield strength to facilitate slip of the slab along the overriding plate. We automatically generate a weak zone of desired thickness following the curvature of the slab from the surface to a desired depth (green in Figure 2). Likewise, we can automatically add oceanic crust of desired thickness to the top of the slab (light blue in Figure 2).

3 Applications

In this section, we present two examples of applications to geological scenarios. Section 3.1 focuses on fault development associated with a salt diapir in an extending regime, including forward simulations and inversion. In section 3.2, we investigate the depen-

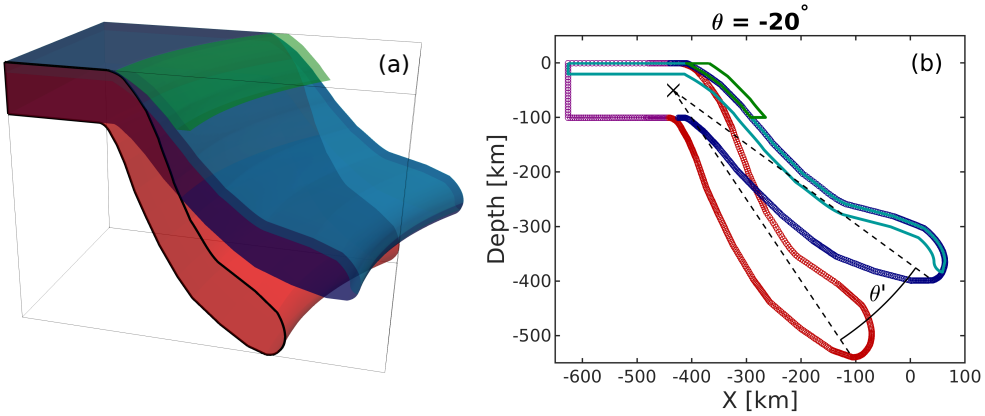

Figure 2. (a) 3D Example of a plate, subducting along a curved trench, drawn in geomIO (red) and an automatically generated variation with reduced subduction angle of 20° (blue). Alongside the variation, we can also automatically generate oceanic crust (light blue) and a weak zone (green) between slab and overriding plate. Black line shows one of the vertical polygons that the 3D volume is represented as inside our algorithm and is identical to the red+purple polygon in 2b. (b) Representation of the plates in 2a as a vertical polygons. Original in red, variation in blue, crust in light blue and weak zone in green. Purple nodes belong to both versions. Black cross shows the center of rotation.

dence of plate velocity on the initial dip angle of a subducting plate and the evolution of the dip angle. Spang et al. (2021) presents a third application to a magmatic system.

3.1 Application I: Salt

Our method is especially useful when constraints from imaging studies are ambiguous like in the case of the Epsilon diapir in Norway (Jackson & Lewis, 2012). After a seismic survey, the stem of the diapir was interpreted to be about 300 m wide (green in Figure 3) but a drilling survey revealed it to be more than 1 km wide instead. Jackson and Lewis (2012) state that the location of the flanks can move hundreds of meters depending on the interpretation of the survey. The authors present a tear-drop-shaped post-drilling interpretation (dashed purple in Figure 3) of the diapir's extent but acknowledge that most of the margins are still uncertain. Jones and Davison (2014) revisit the data on the Epsilon diapir and present a much straighter interpretation (solid purple in Figure 3).

Here, we use the survey of the Epsilon diapir to show how different initial geometries, within the range of uncertainty of imaging data, can result in vastly different model results. We also demonstrate how geodynamic models with variable initial geometries, supported by other observations, can help reduce ambiguity of imaging studies. Figure 3 shows the reflection profile and various interpretations. Without the information of the drilling survey, the red outline could also be a valid interpretation, so we use it as an initial guess and reference model for our variations. The dashed yellow lines show the location of four control polygons located at the basis, the thinnest (neck) and thickest (head) part of the diapir as well as on the transition from neck to head.

3.1.1 Faulting Patterns in Dependence of Initial Geometry

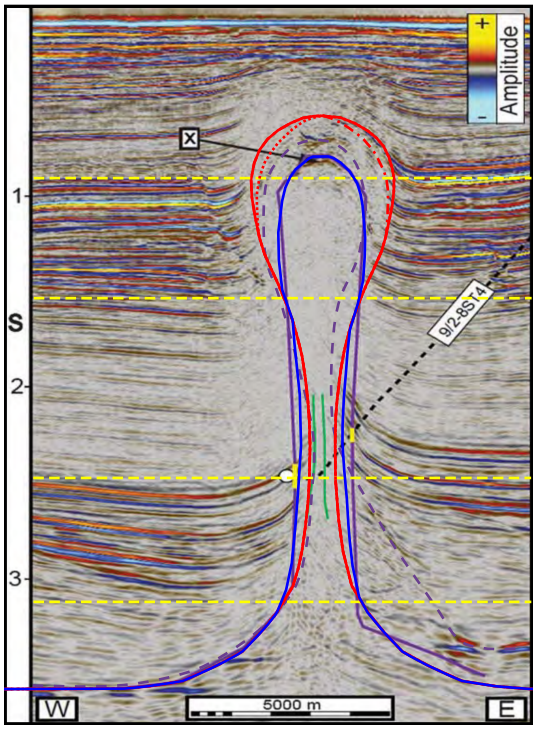

Figure 3. Seismic reflection profile of the Epsilon diapir modified from Jones and Davison (2014). Green lines show pre-drilling interpretation, dashed purple, post drilling interpretation of Jackson and Lewis (2012) and solid purple post-drilling interpretation of Jones and Davison (2014). Red line shows our symmetric initial guess and reference model. Dotted and dashed-dotted red lines show mirrored variations of red to test the effect of asymmetry. Solid blue line shows our synthetic 'true' geometry that we try to fit in section section 3.1.2. Dashed yellow lines show location of control polygons.

Using the red outline in Figure 3 as an initial guess or reference model, we create about 1500 different diapirs. For each variation, we generate a set of scaling parameters (S_1 to S_4) to be applied at the control polygons as well as one parameter (Sz) to vary the height of the diapir. Because it is a 2D example, S_1 to S_4 are equivalent to Sx_1 to Sx_4 and there are no Sy parameters. We generate the scaling parameters on a regular grid within the ranges given in table S3 and add random noise. The reference depth for scaling in the vertical direction is the base of the diapir.

We then model the evolution of each diapir in an extensional geodynamic setting for 100 kyrs, using the thermomechanical code LaMEM (Kaus et al., 2016). We employ a linear-visco-elasto-plastic rheology and a density contrast of 500 $\mathrm{kg\,m^{-3}}$. A more detailed description of the code and the material parameters can be found in supplementary text S2.

From the model output, we binarize the accumulated plastic strain to identify faults that developed to accommodate the extension. With the help of principle component analysis, we extract preferred orientation (α), length (l), aspect ratio (r) and the location (x, z) of the faults or fault systems. The aspect ratio of faults is computed by taking the ratio between the magnitudes of their two principle components (i.e. Eigenvalues).

3.1.2 Inverting for Geometry

With a parameterized geometry, it is possible to invert for the unknown structure of the diapir with the help of an observable. Using a scaling parameter set of 1.2, 2.0, 0.8, 0.6 ($\mathrm{S_1 - S_4}$) and 0.94 (Sz), we produce a synthetic diapir (blue in Figure 3) similar to the interpretation of (Jones & Davison, 2014). We then forward model the evolution of this diapir in an extensional setting for 100 kyrs which results in a single normal fault (Figure 4a). The size, location and orientation of that fault might be visible in a seismic study (Juhlin et al., 2010) and could serve as an observable which we can use to constrain the diapir geometry through inversion.

We compare the faults developed by the 1500 variations to our synthetic observation (fault in Figure 4a, developed by the blue diapir in Figure 3). After identifying the 50 best fitting models, we create 8 new variations with similar parameters for each one to improve our coverage in the area of low misfit (Sambridge, 1999, Neighborhood al-

gorithm). This procedure is commonly used to deal with non-linear and -unique inverse problems (e.g. Baumann & Kaus, 2015) and is repeated four times here, yielding a final ensemble of about 3100 variations. After 2 iterations, it was clear that the minimum for Sx_4 was close to our initial lower bound of 0.5 (table S3) and we relaxed the bound to 0.25 for the 3rd and 4th iteration of the neighborhood algorithm.

Computing a misfit between two geometric observations is not as straight forward as comparing numeric outputs and observations. Wijns et al. (2003) used human appraisal to rank modeled faulting patterns, while Boschetti et al. (2003) utilized self organizing maps to do the same. We compute the misfit of an individual fault pattern, by combining some of the geometric properties of the modeled fault and comparing them to our synthetic observation:

$$\Phi_i = \left(\frac{\sqrt{(|x_i| - |x_o|)^2 + (z_i - z_o)^2}}{l_n} + \frac{||\alpha_i| - |\alpha_o||}{\alpha_n} + \frac{|r_i - r_o|}{r_n} \right) \times N \tag{4}$$

Φ_i is the misfit of a fault to our synthetic observation. Subscript i corresponds to the geometry variation, subscript o to the synthetic observation and subscript n to a normalization constant for each property. The first term of the right hand side compares the location of the fault centers with x corresponding to the lateral and z to the vertical coordinate. α is the angle between the fault and the horizontal direction and r the aspect ratio of the fault. N is the number of faults that develop. We decided to use the absolute values of x and α as section 4.1.1 suggests that the side, to which the faults develop, is not coupled to the geometry. Instead it seems to be related to gridding. l_n is 2 km, a tenth of the model width, α_n is 5° and $r_n = r_o$. These parameters were chosen to make sure that all three right hand side terms are in the range of 0 to 1 for the majority of models. Figure 4 shows how large each of the three terms of equation 4 are for 8 selected fault systems.

3.2 Application II: Subduction

We use the method introduced in section 2.3 to test the dependence of the plate velocity on the initial dip angle (β_0) of the attached slab. Using a reference model, dipping with 60°, we test 16 variations in the range of 30° to 90°. We use a simple 2D model with an oceanic plate of 70 km thickness (corresponding to a thermal age of 30 Myr) subducting underneath a continent of 100 km thickness. Both plates are free (i.e. not fixed

to the edges of the model) and as we do not prescribe any boundary velocities, the movement of the plates in entirely driven by the negative buoyancy of the cold slab. We test models with a 20 km (4 cells) and 30 km (6 cells) wide weak zone. Supplementary text S2 provides more details on the setup and the thermomechanical code we use.

4 Results

4.1 Application I: Salt

4.1.1 Faulting patterns in Dependence of Initial Geometry

We generated about 1500 different salt geometries and modeled the development of faults around them in an extensional environment for 100 kyrs with identical material parameters to investigate the influence of initial geometry on the model results. To accommodate the extension, the models start developing faults at the tip of the diapir as well as the surface. The faults then grow from the surface downwards or from the dipir upwards and eventually connect both (supplementary Figure S4).

In the majority of cases, the strain then focuses on one of the two directions and a single fault forms, taking up most of the deformation. Both sides were preferred in a large number of models for all heights of diapirs (Figure 4b,c). In about 25% of the cases, the fault did not connect to the center of the diapir, but instead it formed at the edges of the diapir top (Figure 4d–h). For some tall diapirs, the deformation did not focus on a single fault but was distributed over an area close to the surface (Figure 4e). In some cases, one dominant fault formed, but parts of the deformation was also accommodated by other parallel and opposite faults (Figure 4g,h). In few cases, two faults formed that shared the strain between them (Figure 4f,i).

By binarizing the plastic strain results, it was possible to automatically detect the faults and parameterize them in terms of preferred orientation (α), aspect ratio (r) and location (x, y). Figure 5 shows a selection of these geometric fault properties in dependence of the scaling parameters applied to the diapir. Supplementary Figure S5 shows all relations between scaling parameters and fault properties.

Intuitively, there is a good correlation between the height of diapir (Sz) and the depth of the lower end of the fault as the fault connects the top of the diapir to the surface (Figure 5a). It is, however, evident that there is some spread towards deeper fault

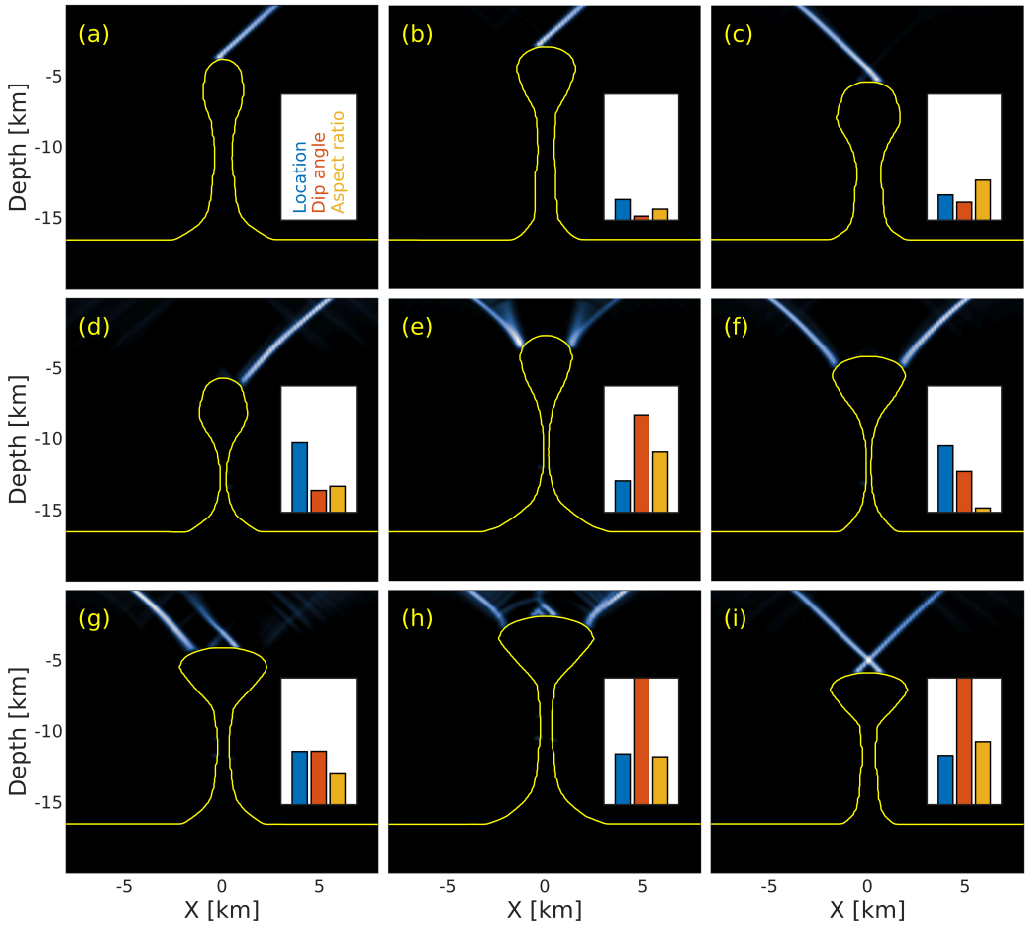

Figure 4. Accumulated plastic strain after 100 kyrs corresponding to normal faults that formed to accommodate the extension of the model. (a) Synthetic 'true' diapir (blue in Figure 3) and corresponding fault which serves as our synthetic observation, other faults are compared to (eq. 4). (b and c) 'Regular case': Deformation focuses on a single fault for different diapir heights. This happens for the majority of cases. (d) Deformation focuses on a single fault but the fault does not start at the center of the diapir top. (e) Deformation is not taken up by a single fault but two areas with a lot of small faults. (f) Faults form on both sides of the diapir. (g) Two parallel faults form with some minor opposite ones. (h) A large number of smaller faults develop. (i) Model develops two crossing faults. Insets show misfit of the observed fault/fault system to the synthetic observation in 4a. Blue bar corresponds to the location term, orange to the orientation term and yellow to the aspect ratio term of equation 4.

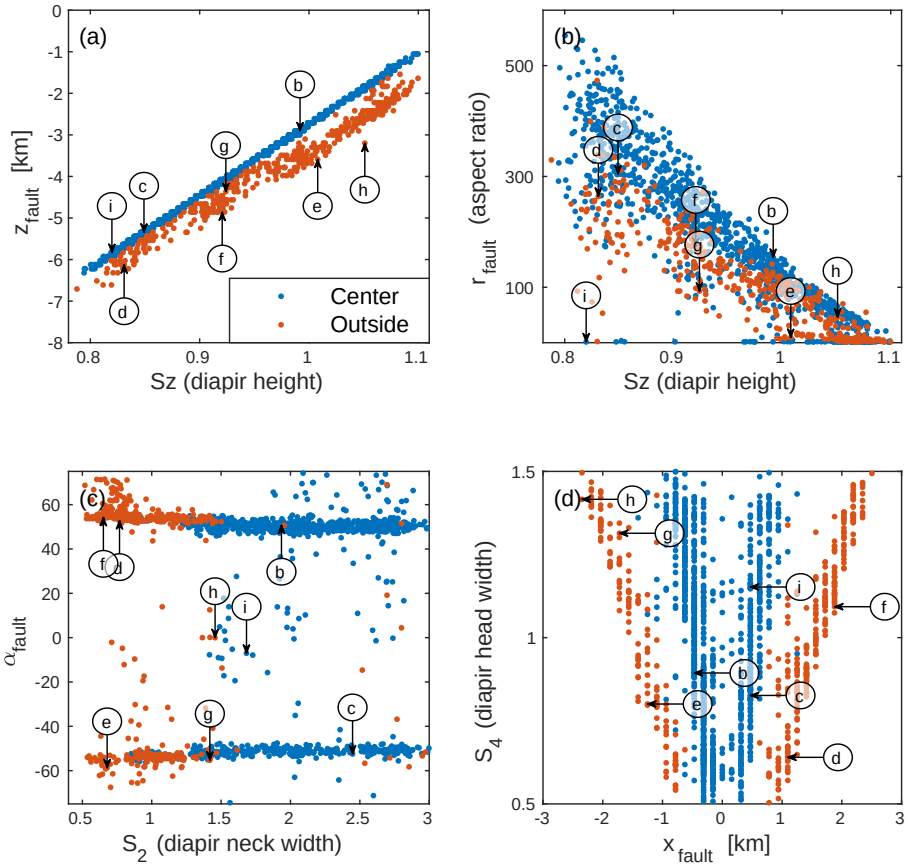

Figure 5. Different fault properties (α, r, x, z) in relation to scaling parameters. (a) Depth of the lower end of the fault in dependence of Sz. This allows for the distinction between faults that start from the center (blue) and faults that start from at the side (orange) of the diapir. Same color code in b–d. (b) Fault aspect ratio in dependence of Sz. (c) Fault orientation in dependence of S_2. $\alpha < 0$: fault goes to the left. (d) Lateral position of the lower end of the fault in dependence of S_4. Arrows show where the examples in Figure 4b–i plot to relate fault types with the parameters.

tips as well. This deviation represents cases where the fault does not start at the tip or center of the diapir, but instead to one of the sides (Figure 4d–h). We use the relation between Sz and the depth of the fault tip to discriminate between two types of faults. The ones that connect to the center of the diapir (blue in Figure 5) and those that connect to the sides (orange).

The aspect ratio scales similarly with Sz as the depth of the fault tip because long faults are not wider than short faults (Figure 5b). The spread is a bit bigger and there are more anomalous cases. Where Sz and r are small, two crossing faults developed (Figure 4i) and the image processing was not able to properly split them, returning flawed values for the width. Cases of low r and large Sz relate to those shown in Figure 4e,h and predominantly happen when the faults do not form in the center of the diapir (orange in Figure 5b).

Figure 5c shows that most faults have an angle of roughly 50 degrees. It also shows a striking dependence of the fault location on S_2 (the neck of the diapir). For small S_2, the faults form almost exclusively to the sides of the diapir (orange) while they occur predominantly in the center (blue) for high S_2. Overall, more faults extend to the right. Given that the diapirs are symmetric, this may be due to small asymmetries that arise from gridding.

Figure 5d relates the width of the diapir head (S_4) and the lateral coordinate of the lower fault tip. It shows that the faults form further from the center, the wider the diapir is. This is the only correlation for S_4 (Figure S5). The figure also clearly shows the two different trends of faults forming in the center or at the sides of the diapir head with few exceptions. S_1 (width of the diapir base) and S_3 (width at transition zone from neck to head of the diapir) do not show any correlation with any of the faults' geometric properties (Figure S5).

4.1.2 Asymmetry

We also tested two sets of models with the same scaling parameters but a slightly asymmetric reference model (red dotted and red dashed-dotted in Figure 3). The asymmetry was introduced by slightly reducing the curvature of the diapir head on one side. As for the symmetric case, we can see a clear distinction between faults that develop from the center of the diapir and those that develop more to the side (Figure 6a,d). But now,

those exclusively develop on one side of the diapir (Figure 6c,f). Mirroring the asymmetry leads to a mirrored result. In all cases, the faults that develop from the side of diapir now appear on the side that retained the original curvature.

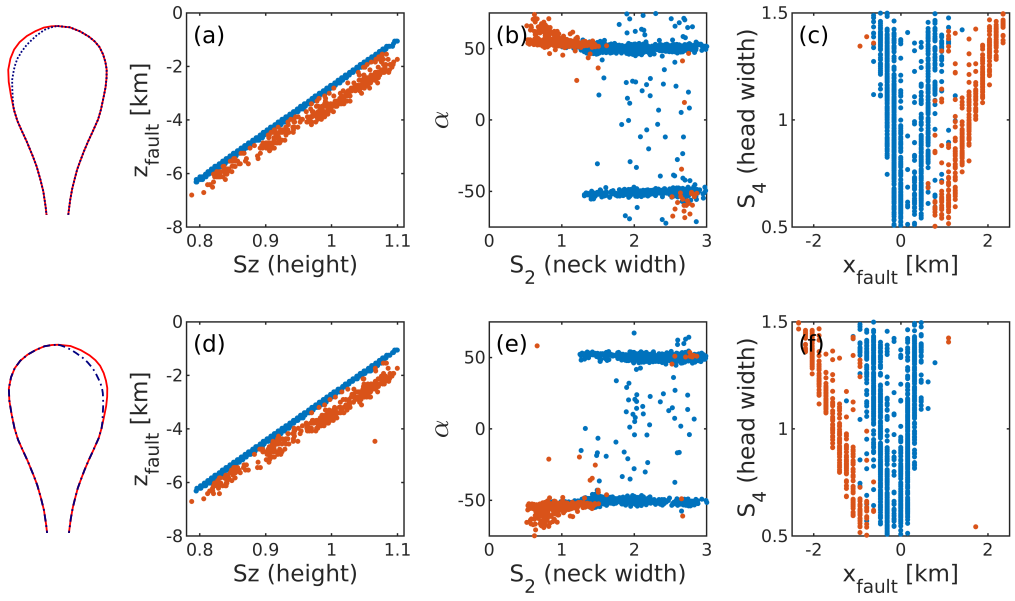

Figure 6. Results for two mirrored asymmetric setups. Upper row has been changed on the left (dotted in Figure 3), lower row on the right (dashed-dotted in Figure 3). Same color code as in Figure 5. (a) and (d) Depth of the lower end of the fault in dependence of Sz. (b) and (e) Fault orientation in dependence of S_2. $\alpha < 0$: fault goes to the left. (c) and (f) Lateral position of the lower end of the fault in dependence of S_4.

4.1.3 Inverting for Geometry

After four iterations of the neighborhood algorithm, we have a total of 3100 models. Figure 7a shows the 200 diapirs that develop faults with the lowest misfit in comparison with the synthetic observation (fault in Figure 4a). All 200 are almost a perfect match for the tip of the diapir in terms of height and shape. The transition between head and neck of the diapir shows very large spread over almost the entire range of possible extents. The neck and base of diapir show less spread but are not as well constrained compared as the top of the diapir.

Figure 7b shows the misfit of each model in dependence of the two most important parameters, the width of the diapir head (S_4) and the height of the diapir (Sz). Sz is the most well defined parameter with models outside the range of 0.9 to 1.0 showing large misfit. But inside that range, there is also a correlation between misfit and S_4 with the minimum in the area of 0.6. As the location of this minimum is very close to our lower bound for Sx_4, we extended it from 0.5 to 0.25 for the last 2 iterations of the neighborhood algorithm.

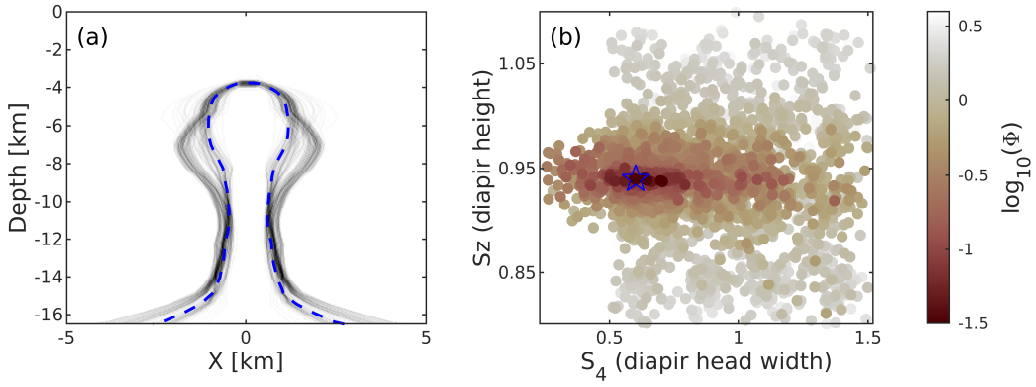

Figure 7. (a) Synthetic diapir in dashed blue (solid blue in Figure 3) and the 200 variations out of 3100 with the smallest misfit in gray. (b) Misfit ($\log_{10}(\Phi)$) as a function of width of the diapir head (S_4) and height of the diapir (Sz). Note the denser distribution of samples around the minimum courtesy of the neighborhood algorithm. Blue star indicates the location of the synthetic 'true' geometry (dashed blue in 7a). Figure S6 shows misfit as a function of all parameter combinations.

4.2 Application II: Subduction

All subduction models start out with an initial stage of slab rollback, trench retreat and continent extension while the slab starts sinking. Over time, the horizontal velocity of the suducting plate increases depending on the angle of the slab (Figure 8). Models that start with a steep subduction angle ($\beta_0 > 65°$) eventually reach a stage where velocities increase strongly and the trench reverses direction and starts to advance towards the continent, leading to shortening of the fore-arc. Once the slab approaches the bottom of the model, velocities decrease again. This also stops the advance of the trench, leading to another rollback period.

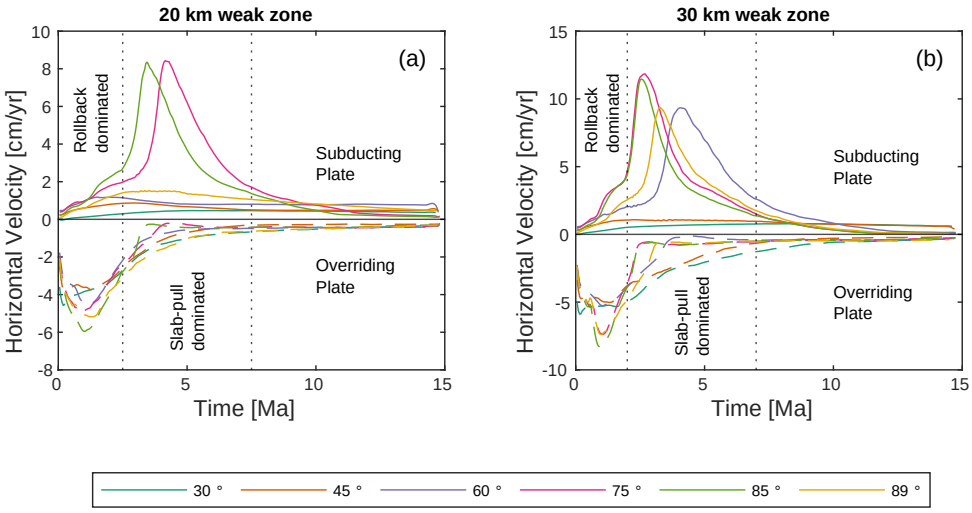

Figure 8. Average velocity of subducting (solid lines in upper panel) and overriding plate (dashed lines in lower panel) in dependence of time for a selection of different initial slab angles (β_0). Dotted vertical lines indicate periods dominated by different mechanisms. Within the first 2.5 Myr, the convergence is mostly accommodated by slab rollback and trench retreat. In the following 5 Myr, it is dominated by the trenchward motion of the subducting plate. (a) Models have a weak zone that is 20 km wide (about 4 grid cells). (b) Models have a weak zone 30 km wide (about 6 grid cells).

Figure S7b shows the velocity field of the reference model ($\beta_0 = 60°$) after 2 Myrs. The plate is moving towards the east and the trench is retreating to the west at the same time. Starting at about 250 km from the trench, a roughly 100 km wide area of extension develops in the continental crust.

4.2.1 Convergence Velocity

In Figure 9a, we show the difference between the average horizontal velocities of subducting and overriding plate (i.e. the convergence velocity) as a function of time and initial subduction angle β_0. Within the first 2 Myr, all models undergo a period of convergence with maximum velocities of 4 $\mathrm{cm\,yr^{-1}}$ for low β_0 and 7 $\mathrm{cm\,yr^{-1}}$ for high β_0. In this period, the convergence velocity is mainly caused by the retreat of the trench (see also Figure 8). For $\beta_0 <= 65°$, the convergence rate then slowly declines over time. However, models that start with a steeper slab go through a second period of rapid accel-

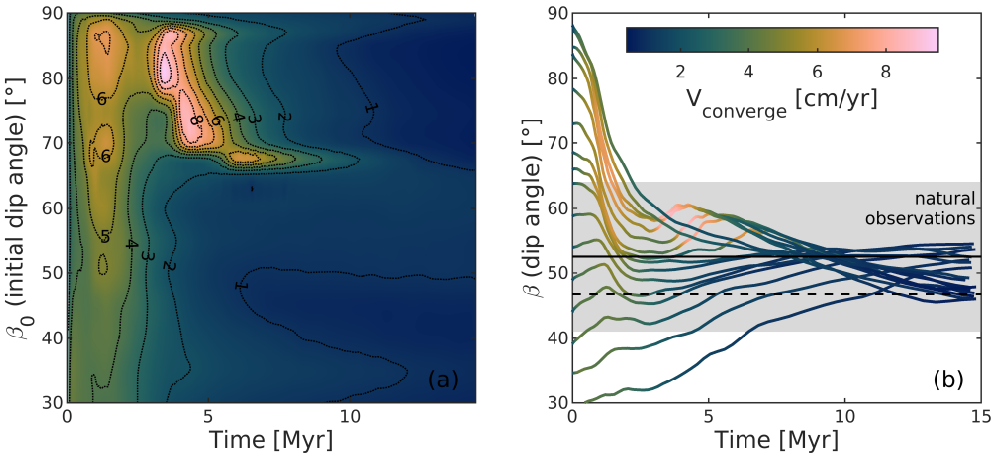

Figure 9. (a) Convergence rate between oceanic and continental plate in dependence of initial subduction angle (β_0) through time. (b) Dip angle of the subducting slab (β) as a function of time for all models. Color gradient along the curves shows convergence velocity. Solid black line shows global average of dip angles from Lallemand et al. (2005) and shaded gray area indicates one standard deviation. Dashed black line shows global average of dip angles from Syracuse and Abers (2006).

eration after about 4 Myr, reaching up to 9 cm yr^{-1} at $\beta_0 = 80°$ before declining as well. In this period, the velocity of the subducting plate is the main contributor to the convergence velocity (Figure 8). While velocities generally increase with β_0, they drastically decrease again at $\beta_0 > 85°$ as we approach a vertical initial slab. Supplementary text S3 presents an example of how a velocity profile can be used to invert for the initial subduction angle β_0 similar to section 4.1.3.

Models with a wider weak zone (30 km instead of 20 km) show the same general behavior, but the velocity of both plates is higher. There are also more models that enter the second phase of acceleration (Figure 8).

4.2.2 Subduction Angle

Figure 9b shows the evolution of the dip angle for all models. While slabs that start out with a shallow dip angle gradually steepen over time, slabs that start steep quickly undergo flattening until leveling out at about 60°. Models that undergo a second phase of acceleration (see Figure 9a) slightly steepen from 55° to 65° during that period again.

Once the slabs start approaching the bottom of the model (660 km depth), they flatten towards 45°. All models converge to a dip angle between 45° and 55° which is agreement with global averages as reported by Lallemand et al. (2005) and Syracuse and Abers (2006).

5 Discussion

5.1 Parameterization and Transformation

The method we present in this study is based on two main concepts. The use of a reference geometry (sphere in section 2.2 and Figure 1, red plate in section 2.3 and Figure 2, red outline in section 3.1 and Figure 3, $\beta_0 = 60°$ model in section 3.2) and control polygons/rotation centers that act as anchors for the transformation.

Using a reference geometry removes the necessity to define a large number of coordinates for every new variation. Instead, each complex shape is represented by a small number of values. This comes at the price of slightly limiting the shape of possible variations (e.g. creating salt diapirs from a spherical reference model is difficult). But as there is usually a rough concept of the shape of the geological unit that is modeled, this limitation is mostly irrelevant.

The use of control polygons and interpolation between them allows us to greatly reduce the number of necessary parameters. Homogeneous three-dimensional scaling of the body is possible with a single control polygon and parameter ($Sx = Sy = Sz$). At the same time, complex changes as shown in Figure 1 can be achieved with only 6 or 7 parameters. Free choice of the position of the control polygons allows for great flexibility. The closer control polygons are to another, the shorter the wavelength of variation. If a part of the geological unit is well constrained, this part can be kept locked by bounding it with two control polygons with constant scaling parameters of 1, while the other parts can stay variable.

Our approach enables the user to quickly, on the order of a second per version, and automatically create any number of variations of a complex 3D body in their model. This not only allows for the incorporation of uncertain constraints but can also reveal unexpected dependencies of the model results on the initial geometry of the model. The scaling parameters even facilitate a quantitative description of such dependencies.

5.2 Application to Salt

Figure 4 shows that different initial geometries within the range of uncertainty of geophysical imaging can lead to drastically different modeling results. Therefore, it is crucial to test different setups and develop an understanding of the influence that the geometry of the geological structures can have. In the case of the salt diapir, we observe some intuitive relationships like the link between height of the diapir and position or aspect ratio of the fault (Figure 5a,b). But, we also find unexpected correlations like a thin diapir neck facilitating faults at the sides of the diapir (Figure 5c). We also learn that the base of the diapir (S_1) and the transition from head to neck (S_3) have little to no impact on the developing faults and could therefore be kept constant in further investigations of the system. It is apparent that faults can develop to both sides of the diapir independently of the geometry for the symmetric diapir. A slight preference for faults to the right suggests that the gridding of the model might play a minor role in determining the direction of the fault.

Introducing a slight asymmetry into our reference model by steepening one side, drastically influences the results. We still observe faults that extend from the center of the diapir and faults that start at its side (Figure 6a,d). But while the ones extending from the center still go into both directions, the ones that develop at the side of the diapir are exclusively on the side that has a stronger curvature (Figure 6c,f). We tested the asymmetry on both sides to exclude the possibility that this effect is caused by our grid discretization.

Finally, we can see that, given the observation of a fault and a good understanding of the material parameters, geodynamic modeling could help improve imaging results and reduce ambiguity regarding the extent of a diapir. Figure 7 shows that it is possible to very precisely invert for the height and tip geometry of a diapir while deeper structures that have no influence of the faulting pattern remain blurred. Even with the solution at the edge of our sampling domain, we are able to constrain S_4 well.

5.3 Application to Subduction

Our models show the typical features (trench retreat, slab rollback, backarc extension) that have been observed in many previous numerical and analogue models (e.g. Gerya, 2011; Meyer & Schellart, 2013; Schellart & Moresi, 2013; Holt et al., 2015). Like Holt

et al. (2015), we observe extension in the overriding plate despite the lack of toroidal (horizontal) flow around the edges of the subducting plate. The location of maximum extension is at about 250 km distance from the trench which is in line with analogue experiments (Meyer & Schellart, 2013; Chen et al., 2015).

Figures 8 and 9a show how strongly the velocity of plates and the entire dynamics of the model depend on the initial angle of the subducting slab. While models with an initial angle $\beta_0 <= 65°$ move at relatively even velocities throughout 15 Myr, models with steeper slabs run through a period of strongly increasing velocities that are high enough to stop or even reverse the retreat of the trench. The timing and maximum velocity of this phase of acceleration also depend on the initial geometry of the model.

Another geometrical parameter that strongly influences the velocities of the plates is the thickness of the weak zone between subducting and overriding plate (Figure 8). With a thicker weak zone, there is less friction between the plates and they reach higher velocities. So, both parameters (initial dip angle of the slab and thickness of the weak zone) can exert a first order control on the model dynamics and could overprint a lot of other effects. The dependency of results on these parameters should be investigated when subduction is modeled. With our method, it is easy to change either parameter and investigate their influence on the model results without investing a lot of time into creating different initial geometries.

Figure 9b shows that independently from the initial subduction angle (β_0), all models converge to a similar angle of about 50° after a few Myr. Counter intuitively, models with a low β_0 converge to a slightly higher angle than those with a high β_0. This is due to the fact that by the end of our simulation time, the slow moving moving low β_0 slabs have not interacted with the bottom of the model (660 km) yet while the fast subducting models with a high β_0 were forced to flatten once they approached the bottom. The fact that all our models converge to angles that are in agreement with global averages of subucting slabs (Lallemand et al., 2005; Syracuse & Abers, 2006) suggests that 50° is the preferred angle for long-term slab-pull-dominated subduction.

6 Conclusion

In this study, we present a simple and intuitive method to describe and manipulate 3D bodies in a heterogeneous manner with a limited set of parameters. This not only

allows us to include uncertainties about initial geometry in the modeling process, but also enables us to quantify the relationship between initial geometry of a model and the computed output. As shown by our study and Spang et al. (2021), this allows us to even improve constraints on geometry by integrating different observations and invert for geometric properties.

We present two application examples. (i) A salt diapir with an ambiguous geometry in seismic imaging. We show that slight geometric variations that would all satisfy the imaging data, can result in the development of vastly different faulting patterns in an extending regime. It is also evident that small asymmetries in the diapir lead to distinctive differences in the developing faults around the diapir. Furthermore, we show that, given sufficient observations, we are able to invert for the geometric properties that the observation is sensitive to. (ii) A subduction zone where we vary the initial dip angle of the subducting slab as well as the thickness of the weak zone between subducting and overriding plate. Both parameters influence the velocity evolution of the plates by an order of magnitude. We show that, independently of the initial dip angle, all slabs approach a subduction angle of about 50°.

Our study presents a new tool to parameterize initial geometry and highlights the importance to do so. Other areas of applications include studies on volcanic systems with varying sizes/shapes of magma bodies, models of orogenesis with uncertain extents of critical units as well as gravity, magnetotellurics and seismic tomography. The tool is available through the open-source software package geomIO which is fully compatible with the open-source, thermomechanical stokes code LaMEM. Horizontal scaling as outlined in section 2.1.3 is directly implemented in LaMEM.

Acknowledgments

This study was funded by the European Research Council through the MAGMA project, ERC Consolidator Grant # 771143. We used perceptually uniform colormaps to prevent optical data distortion (Crameri, 2018). Parts of this research were conducted using the supercomputer Mogon II and/or advisory services offered by Johannes Gutenberg University Mainz (hpc.uni-mainz.de), which is a member of the AHRP (Alliance for High Performance Computing in Rhineland Palatinate, www.ahrp.info) and the Gauss Alliance e.V..

Open Research Section

Software for this research is available on zenodo at:

- LaMEM (Kaus et al., 2016): http://doi.org/10.5281/zenodo.5714513
- geomIO (Bauville & Baumann, 2019): http://doi.org/10.5281/zenodo.5717846

References

Baumann, T. S., & Kaus, B. J. P. (2015). Geodynamic inversion to constrain the non-linear rheology of the lithosphere. *Geophysical Journal International*, *202*(2), 1289–1316.

Baumann, T. S., Kaus, B. J. P., & Popov, A. A. (2014). Constraining effective rheology through parallel joint geodynamic inversion. *Tectonophysics*, *631*, 197–211. doi: https://doi.org/10.1016/j.tecto.2014.04.037

Bauville, A., & Baumann, T. S. (2019). geomIO: an open-source MATLAB toolbox to create the initial configuration of 2-D/3-D thermo-mechanical simulations from 2-D vector drawings. *Geochemistry, Geophysics, Geosystems*, *20*(3), 1665–1675. doi: https://doi.org/10.1029/2018GC008057

Boschetti, F., Wijns, C., & Moresi, L. (2003). Effective exploration and visualization of geological parameter space. *Geochemistry, Geophysics, Geosystems*, *4*(10).

Chen, Z., Schellart, W. P., & Duarte, J. C. (2015). Overriding plate deformation and variability of fore-arc deformation during subduction: Insight from geodynamic models and application to the Calabria subduction zone. *Geochemistry, Geophysics, Geosystems*, *16*(10), 3697–3715.

Crameri, F. (2018). Scientific colour-maps. *Zenodo*, *10*. doi: 10.5281/zenodo.1243862

Galley, C. G., Lelièvre, P. G., & Farquharson, C. G. (2020). Geophysical inversion for 3d contact surface geometry. *Geophysics*, *85*(6), K27–K45.

Gerya, T. (2011). Future directions in subduction modeling. *Journal of Geodynamics*, *52*(5), 344–378.

Holt, A., Becker, T., & Buffett, B. (2015). Trench migration and overriding plate stress in dynamic subduction models. *Geophysical Journal International*,

201(1), 172–192.

Jackson, C. A.-L., & Lewis, M. M. (2012). Origin of an anhydrite sheath encircling a salt diapir and implications for the seismic imaging of steep-sided salt structures, Egersund Basin, Northern North Sea. *Journal of the Geological Society*, *169*(5), 593–599. doi: 10.1144/0016-76492011-126

Jones, I. F., & Davison, I. (2014). Seismic imaging in and around salt bodies. *Interpretation*, *2*(4), SL1–SL20. doi: 10.1190/INT-2014-0033.1

Juhlin, C., Dehghannejad, M., Lund, B., Malehmir, A., & Pratt, G. (2010). Reflection seismic imaging of the end-glacial Pärvie Fault system, northern Sweden. *Journal of Applied Geophysics*, *70*(4), 307–316.

Kaus, B. J. P., Popov, A. A., Baumann, T., Pusok, A., Bauville, A., Fernandez, N., & Collignon, M. (2016). Forward and inverse modelling of lithospheric deformation on geological timescales. In *Proceedings of NIC Symposium.*

Lallemand, S., Heuret, A., & Boutelier, D. (2005). On the relationships between slab dip, back-arc stress, upper plate absolute motion, and crustal nature in subduction zones. *Geochemistry, Geophysics, Geosystems*, *6*(9).

Meyer, C., & Schellart, W. P. (2013). Three-dimensional dynamic models of subducting plate-overriding plate-upper mantle interaction. *Journal of Geophysical Research: Solid Earth*, *118*(2), 775–790.

Ratnaswamy, V., Stadler, G., & Gurnis, M. (2015). Adjoint-based estimation of plate coupling in a non-linear mantle flow model: theory and examples. *Geophysical Journal International*, *202*(2), 768–786.

Reuber, G. S., Kaus, B. J. P., Popov, A. A., & Baumann, T. S. (2018). Unraveling the physics of the Yellowstone magmatic system using geodynamic simulations. *Frontiers in Earth Science*, *6*, 117. doi: 10.3389/feart.2018.00117

Sambridge, M. (1999). Geophysical inversion with a neighbourhood algorithm-I. Searching a parameter space. *Geophysical Journal International*, *138*(2), 479-494. doi: 10.1046/j.1365-246X.1999.00876.x

Schaaf, A., de la Varga, M., Wellmann, F., & Bond, C. E. (2021). Constraining stochastic 3-D structural geological models with topology information using approximate Bayesian computation in GemPy 2.1. *Geoscientific Model Development*, *14*(6), 3899–3913.

Schellart, W. P., & Moresi, L. (2013). A new driving mechanism for backarc exten-

sion and backarc shortening through slab sinking induced toroidal and poloidal mantle flow: Results from dynamic subduction models with an overriding plate. *Journal of Geophysical Research: Solid Earth*, *118*(6), 3221–3248.

Sevilla, R., Zlotnik, S., & Huerta, A. (2020). Solution of geometrically parametrised problems within a cad environment via model order reduction. *Computer methods in applied mechanics and engineering*, *358*, 112631.

Spang, A., Baumann, T., & Kaus, B. (2021). A Multiphysics approach to constrain the dynamics of the Altiplano-Puna magmatic system. *Journal of Geophysical Research: Solid Earth*, *126*, e2021JB021725.

Syracuse, E. M., & Abers, G. A. (2006). Global compilation of variations in slab depth beneath arc volcanoes and implications. *Geochemistry, Geophysics, Geosystems*, *7*(5).

Varga, M. D. L., Schaaf, A., & Wellmann, F. (2019). GemPy 1.0: open-source stochastic geological modeling and inversion. *Geoscientific Model Development*, *12*(1), 1–32.

Wijns, C., Boschetti, F., & Moresi, L. (2003). Inverse modelling in geology by interactive evolutionary computation. *Journal of Structural Geology*, *25*(10), 1615–1621.

585 **Supporting Information References**

586 ## References

587 Baumann, T. S., Kaus, B., & Popov, A. A. (2018). Deformation and stresses related
588 to the gorleben salt structure: insights from 3d numerical models. *Mechanical*
589 *Behavior of Salt, Saltmech IX*, 15–27.

590 Crameri, F., Schmeling, H., Golabek, G. J., Duretz, T., Orendt, R., Buiter, S., ...
591 Tackley, P. (2012). A comparison of numerical surface topography calculations
592 in geodynamic modelling: an evaluation of the 'sticky air'method. *Geophysical*
593 *Journal International*, *189*(1), 38–54.

594 Drucker, D. C., & Prager, W. (1952). Soil mechanics and plastic analysis or limit de-
595 sign. *Quarterly of applied mathematics*, *10*(2), 157–165.

596 Harlow, F. H., & Welch, J. E. (1965). Numerical calculation of time-dependent vis-
597 cous incompressible flow of fluid with free surface. *The physics of fluids*, *8*(12),
598 2182–2189.

599 Ingraham, M. D., Broome, S. T., Bauer, S. J., Barrow, P. C., & Flint, G. M. (2015,
600 June). Behavior of salt from the bayou choctaw salt dome. In *49th us rock me-*
601 *chanics/geomechanics symposium.*

602 Kaus, B. J. P., Mühlhaus, H., & May, D. A. (2010). A stabilization algorithm for
603 geodynamic numerical simulations with a free surface. *Physics of the Earth*
604 *and Planetary Interiors*, *181*(1-2), 12–20.

605 Martinod, J., Husson, L., Roperch, P., Guillaume, B., & Espurt, N. (2010). Hori-
606 zontal subduction zones, convergence velocity and the building of the Andes.
607 *Earth and Planetary Science Letters*, *299*(3-4), 299–309.

608 Sdrolias, M., & Müller, R. D. (2006). Controls on back-arc basin formation. *Geo-*
609 *chemistry, Geophysics, Geosystems*, *7*(4).

610 Zong, J., Stewart, R. R., Dyaur, N., & Myers, M. T. (2017). Elastic properties of
611 rock salt: Laboratory measurements and gulf of mexico well-log analysis. *Geo-*
612 *physics*, *82*(5), D303–D317.